# Surface Chemistry, Structure, and Electronic Properties from Microns to the Atomic Scale of Axially Doped Semiconductor Nanowires

Martin Hjort,[†] Jesper Wallentin,[†] Rainer Timm,[†] Alexei A. Zakharov,[‡] Ulf Håkanson,[†] Jesper N. Andersen,[†,‡] Edvin Lundgren,[†] Lars Samuelson,[†] Magnus T. Borgström,[†] and Anders Mikkelsen[†,*]

[†]Nanometer Structure Consortium (nmC@LU) and [‡]MAX IV Laboratory, Lund University, P.O. Box 118, 221 00 Lund, Sweden

ABSTRACT Using both synchrotron-based photoemission electron microscopy/spectroscopy and scanning tunneling microscopy/spectroscopy, we obtain a complete picture of the surface composition, morphology, and electronic structure of InP nanowires. Characterization is done at all relevant length scales from micrometer to nanometer. We investigate nanowire surfaces with native oxide and molecular adsorbates resulting from exposure to ambient air. Atomic hydrogen exposure at elevated temperatures which leads to the removal of surface oxides while leaving the crystalline part of the wire intact was also studied. We show how surface chemical composition will seriously influence nanowire electronic properties. However, opposite to, for example, Ge nanowires, water or sulfur molecules adsorbed on the exterior oxidized surfaces are of less relevance. Instead, it is the final few atomic layers of the oxide which plays the most significant role by strongly negatively doping the surface. The InP nanowires in air are rather insensitive to their chemical surroundings in contrast to what is often assumed for nanowires. Our measurements allow us to draw a complete energy diagram depicting both band gap and differences in electron affinity across an axial nanowire p-n junction. Our findings thus give a robust set of quantitative values relating surface chemical composition to specific electronic properties highly relevant for simulating the performance of nanoscale devices.
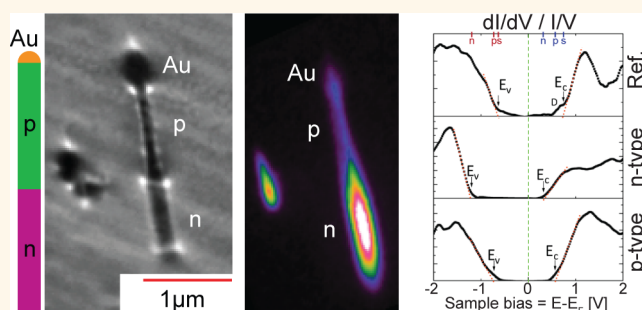
KEYWORDS: nanowires · STM · surface · PEEM · III—V · oxide · XPS

The control of semiconductor nanowire (NW) electronic properties, *via* impurity incorporation during synthesis, has been studied extensively in recent years.[1−3] However, the exact surface chemistry and composition and its influence on electronic properties remains largely unexplored with only a few sporadic studies.[4,5] This is especially unfortunate, as not only do the NWs represent a technologically highly relevant system[6,7] but the opportunities for axial doping also make the direct comparison between differently doped regions on the nanoscale easily accessible. Chemical vapor deposition (CVD)-synthesized III—V semiconductor NWs are currently being explored as key building blocks for high-efficiency photovoltaics,[8] light-emitting diodes (LEDs),[9] and a variety of electronic devices.[10] A central issue is the control over the NW surface, that is, its chemistry and morphology, which can seriously affect device functionality.[11−13] Surface chemistry and structure will often induce surface states leading to band bending reaching far into the NW, reducing the effect of doping.[14] In addition, any attempt to extract or inject electrons *via* contacts to the surface of the NW leads to questions on the surface electron affinity. Finally, defects at the surface can act as electron/hole traps, reducing the efficiency of most photonic devices, even though positive effects also have been reported.[15] To understand the influence of the surface, a complete picture of the surface chemistry, structure, and composition needs to be directly correlated with the surface electronic properties. However, atomically resolved surface studies on III—V NWs have shown to be an experimental challenge, and very

few publications have been presented so far.[16,17] While the very significant influence of NW surfaces on doping has been acknowledged in a number of important cases *via* indirect methods,[3,11,18−20] no studies of NWs exist where their complete surface composition and structure have been thoroughly and directly mapped out. Especially disconcerting is the observation that on Ge NWs both the native oxide and also water (invariably) adsorbed on the NWs when they are exposed to the ambient air can seriously influence electronic properties.[4] In order to control the influence of the surface in III−V electronics, two general concepts have been to remove the native oxide (formed upon exposing the semiconductor to air) and replace it with a passivating chemistry using, for example, ammonium sulfide ($(NH_4)_2S_x$), presumably leading to a sulfur passivation,[21] or using metal organic species in combination with water to grow a dielectric *via* atomic layer deposition.[22] This is reminiscent of the role of SiO_2 on Si, which can be chemically engineered to have an extremely small number of active interface defects.

A central starting point for any systematic investigation of the influence of the surface chemistry on the electronic properties is the clean surface without the native oxide. This is a delicate point, especially for the compound semiconductors, which often have a lower melting point than bulk structures, as the removal of the native oxide can lead to decomposition of the nanostructure. In the present paper, we have chosen the InP axial p-n junction NW as our fundamental system of study, as this constitutes an important component for future photovoltaic applications and is explored to a considerable degree for the possibility to synthesize an axially doped version of the NWs in a controlled fashion.[8,23] Thus, significant knowledge and interest in this system exists beforehand. Removal of the surface oxide and other adsorbates on the surface of bulk InP has been studied to some extent previously,[24−26] where it has even been indicated that removal of the oxide using atomic hydrogen and subsequent careful reoxidation could be a starting point for a high-quality surface.

In this article, we report on the use of X-ray-induced secondary electron (SE) imaging to measure charge carrier concentrations in doped InP NWs composed of axially stacked n and p-type segments. Core level photoelectrons were used for imaging with surface chemical sensitivity as well as for spectroscopy using high-resolution X-ray photoelectron emission microscopy/spectroscopy (XPEEM/XPS). Low-energy electron microscopy/mirror electron microscopy (LEEM/MEM) was used in order to obtain information about the morphology of the sample quickly. Scanning tunneling microscopy/spectroscopy (STM/S) was used to obtain both structural as well as electronic properties of the NWs with down to single nanometer precision. This allows us to finally present a complete

picture of the NW surfaces both in a clean state and with native oxide.

RESULTS AND DISCUSSION

We start by evaluating the overall NW chemistry and effect on band bending with and without a surface oxide. In Figure 1a, we show XPS phosphorus 2p spectra recorded for 80 nm thick p-type InP NWs with the native oxide after prolonged ambient air exposure and spectra after removal of the native oxide by annealing in atomic hydrogen. From LEEM and XPEEM measurements on the NWs, we have observed desorption of volatile species after electron or photon bombardment. Thus we conclude that moisture-related species from the air have also been adsorbed on the NW surfaces. High-resolution XPS spectra were recorded using photoelectrons excited with 250 eV photons, resulting in a very high surface sensitivity. At around 128 eV in binding energy, we observe the two spin−orbit 2p components of P bound to In in bulk InP. The sharp peaks are an indication of the crystalline nature of the NWs. The broad feature around 133 eV contains the spin−orbit 2p components of P in the native oxide. Comparing the two spectra in Figure 1a, we note that the P-related oxides are removed by the hydrogen treatment already after four cleaning cycles. The position and 2 eV full width at half-maximum (fwhm) of the oxide component in the P2p spectra is indicative of the presence of several P suboxides. The shift of the oxide peaks compared to bulk InP P2p is known from previous studies[24,26,27] to be $InPO_4$ (ΔBE = 5.3 eV), $InPO_3$ (ΔBE = 4.7 eV), $In(PO_3)_3$ (ΔBE = 4.9 eV), and P_2O_5 (ΔBE = 6.8 eV). Thus, from the position of the oxide peak at +4.9 and its fwhm of 2 eV, we conclude that we have a mixture of InP_xO_y states, but not the highly shifted P_2O_5. From spectra of In3d seen in Figure 1b, we see that, although the peaks belonging to oxide and bulk partly overlap, it is clear that the In−O components have also been mostly removed by the hydrogen treatment. A quantitative fit of the In3d spectra indicates that the In oxides are reduced to less than 10% of their initial amount after one treatment. The remaining oxide is also in a lower oxidation state than most of the original native oxide.

Further, we find that the peaks belonging to the InP have shifted by 0.42 eV after the anneal, as is most clearly seen in Figure 1a. This shift in binding energy is associated with a shift of the Fermi level because the surface band bending is significantly reduced. The measurements show that the InP oxides pin the Fermi level close to the conduction band, in agreement with bulk InP studies.[26] This indicates that oxide removal leads to at least partial removal of the surface band bending. Below, we can define the actual position more closely as we determine the bandstructure using STS. As this oxide-induced band bending is quite strong, this will affect also the interior of the NW, and
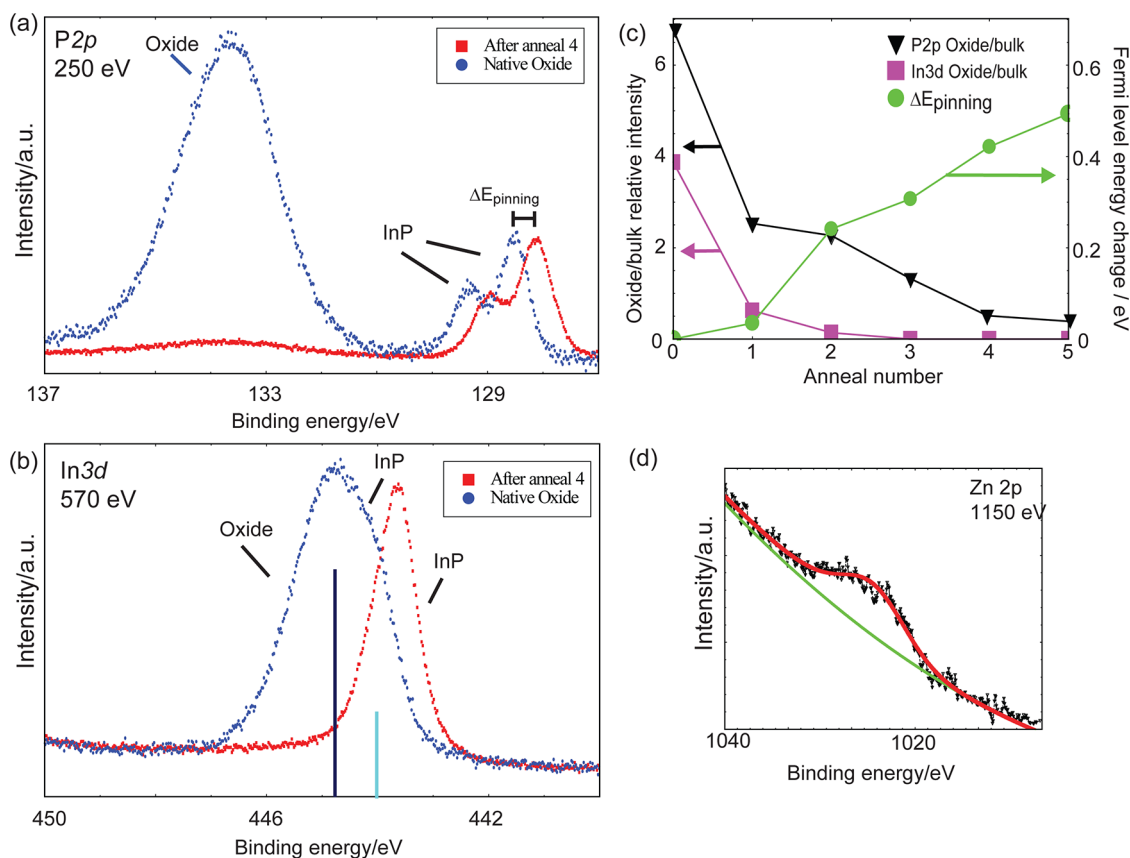
Figure 1. XPS results from the cleaning of homogenously doped p-type InP NWs. (a) P2p spectra depicting the two spin−orbit components (around 129 eV) as well as the broad oxide peak (around 134 eV) for uncleaned (blue) and hydrogen-cleaned (red) NWs. Spectra were obtained using 250 eV photons. The energy shift of the whole spectrum from the oxidized to the clean surface ($\Delta E_{pinning}$) is due to the change in the Fermi level as the surface pinning is partially lifted by removal of the oxide. (b) In3d spectra from the same sample as in (a) showing uncleaned (blue) and cleaned (red) NWs. For this core level, the oxide and InP components are only separated by 1−2 eV. Still, in the uncleaned (blue) spectrum, the appearance of the strong oxide peak (indicated by the dark blue line) and the InP-related peak (indicated by the light blue line) can be identified. Spectra were obtained using 570 eV photons, that is, the same photoelectron kinetic energy as in panel a. (c) Reduction of surface P oxides (black) and In oxides (red) together with the corresponding change in Fermi level energy (green) is shown *vs* the number of cleaning cycles. (d) Zn2p$_{3/2}$ peak from measurements on p-type InP NWs with 80 nm diameter obtained using X-rays with a photon energy of 1150 eV.

as a result, a significant portion of the uncleaned NWs will be n-type, as discussed in more detail below. It is seen that removal of the first layers of oxides and also different adsorbed species on the surface leads only to a minor change of the surface pinning. Thus, in contrast to Ge NWs, where water on the surface has a significant influence,[26] this is not the case for the InP NWs. We have also tested the influence of ammonium sulfide wet chemical treatments in the same fashion and found that again sulfur termination of the surface results in only a minor release of the pinning of the surface. Generally, we can conclude that the change in pinning is mostly correlated with the removal of phosphorus-dominated oxides closest to the NW. In Figure 1c, we summarize the results for the p-type NWs. With these measurements, it is also possible to obtain a quantitative measure of the amount of various chemical species at the surface.[5] Here we use that the ratio of the In3d and P2p components originating from the interior of the NW must be equivalent to a 1:1 In/P ratio.

This allows us to make an estimate of the oxide composition without using the somewhat uncertain cross sections of the materials. To estimate the oxide thickness, we use tabulated values for the mean free path.[5] We conclude that the native oxide has a composition with a P to In ratio of 1.8, and that the thickness is around 9−10 atomic layers. Interestingly, the observation of more P oxides than In oxides is in contrast to InAs NWs, where we instead have an excess of indium in the oxides.[5] We also investigated n-type NWs with a diameter of 15 nm (Sn-doped). The native oxide could again be removed, and a shift of −0.15 eV in binding energy was observed. This shift indicates that the band bending induced by the native oxide results in an even stronger n-type character of the NWs than the already significant intentional n-doping. The oxidation states of phosphor in the n-type NWs were generally lower. While the amount of phosphor in the oxides was similar between the two types of doped NWs, the amount of indium in the oxides was roughly

twice as large for the p-type NWs. These differences could be attributed to a number of factors such as the presence of the dopant atoms on the surface or the different crystal structures for n-type (Wz) and p-type (Zb). Even without the structural differences, oxidation might be different for p- and n-type materials as was observed for Ge NWs[4] and for planar Si substrates.[28] As a note, we also observed a shift of −0.1 eV for 80 nm n-type (S-doped) NWs.

The high photon flux from the synchrotron even allowed for detection of Zn dopant atoms at the surface of the homogenously doped p-type NWs (see Figure 1d). We obtained a much higher abundance of Zn in the surface than what was estimated from electrical measurements of the bulk of the NWs.[29] Zn was observed both for oxide-covered and hydrogen-cleaned NWs. Using tabulated values for the photo-ionization cross sections for the In3d and Zn2p peaks,[30] we conclude that a Zn coverage of 0.2 monolayer fits well with the observed In3d and Zn2p intensities. The high amount of surface-related Zn should be compared to a previous report by van Weert et al., who studied similar InP p-n NWs and found that the Zn dopants existed in the core of the NWs.[2] Further, it is interesting to note that Zn dopants in InP have been observed to desorb from the surface rather than to accumulate,[31] which can be an indicator that the amount of surface Zn was even higher immediately after growth. Thus we conclude that, while Zn incorporation into the NW through the Au particle seed[2] is possible, a significant amount of Zn will also be present at the surface of the NW.

We continue by mapping out the detailed structure and morphology along the NW using STM. Here we especially focus on the NWs after hydrogen cleaning, which we know from XPS to give a surface with significantly less than 1 monolayer oxide. In Figure 2a, we present a large-scale STM image depicting an axial p-n junction InP NW grown from 80 nm Au aerosol particles (same NWs as presented in ref 29). In the overview image, the difference in crystal structure of the bottom n-part and the top p-part is clearly indicated by the change of the NW morphology. On one part, a periodic corrugation of 20 Å in height was observed with a spacing of 200 Å (Figure 2b,d), which is inherent to the twinned Zb structure, often observed in p-type InP NWs.[32] From previous studies including transmission electron microscopy (TEM) results on identically grown Zn-doped InP NWs, we can identify this morphology belonging to the p-doped part of the NW.[29] For the n-part (Figure 2c,e), we obtain small terraces with local height differences in the 5−10 Å range, which we can then assign as the morphology of the dominating Wz stacking in that part of the NW, again in perfect agreement with TEM data.[29] The atomic scale surface structure on the NWs appeared only semiordered. A closer look on the n-part, as shown
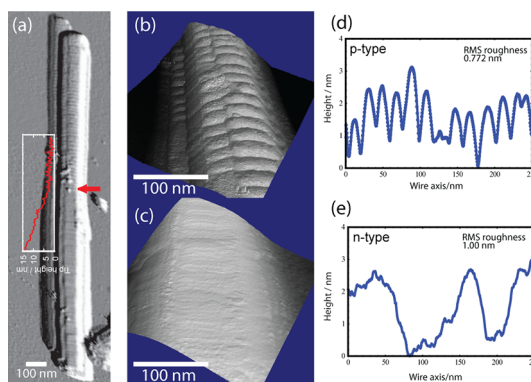

Figure 2. InP p-n junction NW imaged by STM. (a) Large-scale image of a pn-NW; the red arrow marks the transition between the n-part (bottom) and the p-part (top) as seen by a change of NW morphology from Wz to twinned Zb. Please note that what appears to be a second NW at the left-hand side is merely an artifact from a double tip. The image has been differentiated for ease of viewing, $U_{sample} = -3.0$ V. Inset shows the corrugation along the transition. (b) The p-part of the pn-NW showing the twinned Zb structure, $U_{sample} = -3.0$ V. (c) The n-part of the pn-NW with predominantly Wz stacking, $U_{sample} = -3.0$ V. (d,e) Line profiles along the p- and n-type parts, respectively.

in Figure 3a, revealed disordered atomic rows extending perpendicular to the NW growth axis with a row spacing of 20 Å, which is indicative of a reconstruction of the surface. This is in contrast to our previous observations of no reconstructions on InAs Wz NW surfaces.[17] Thus, if the surfaces are well-ordered, we will see this very clearly in our STM. This leads us to conclude that these Wz InP NW surfaces must to a large extent be disordered on the atomic scale beyond the row structure observed on the n-part. The observed row-like structures on the NWs could be evidence of a dimerization of the surface as is observed on a number of III−V surfaces.[33,34] A similar difference in the behavior is observed by us when comparing the InP(111) and InAs(111) substrate structures. Here also InP(111) appears with a semiordered reconstruction (Figure 3d,e), in comparison to the ordered and unreconstructed InAs(111) surface.[35] The p-part of the NW, which consists of small InP(111) facets with various orientation, shows a similar semidisordered structure as the InP-(111)B substrate. In this case, what one is observing is presumably In or P trimers which cannot form an ordered structure that fits with the underlying substrates and thus forms a semirandom pattern. Such trimers have been observed on other III−V surfaces.[36] On a large InP(111) surface, some longer scale ordering of these trimers nonetheless is observed; however, on the very small terraces of the nanowires, no such ordering can be expected.

To gain a further understanding of the surface electronic properties, we performed STS on different axial positions along the pn-NWs after removal of the surface oxide. Care was taken to position the tip at areas free of any structural defects, small remaining
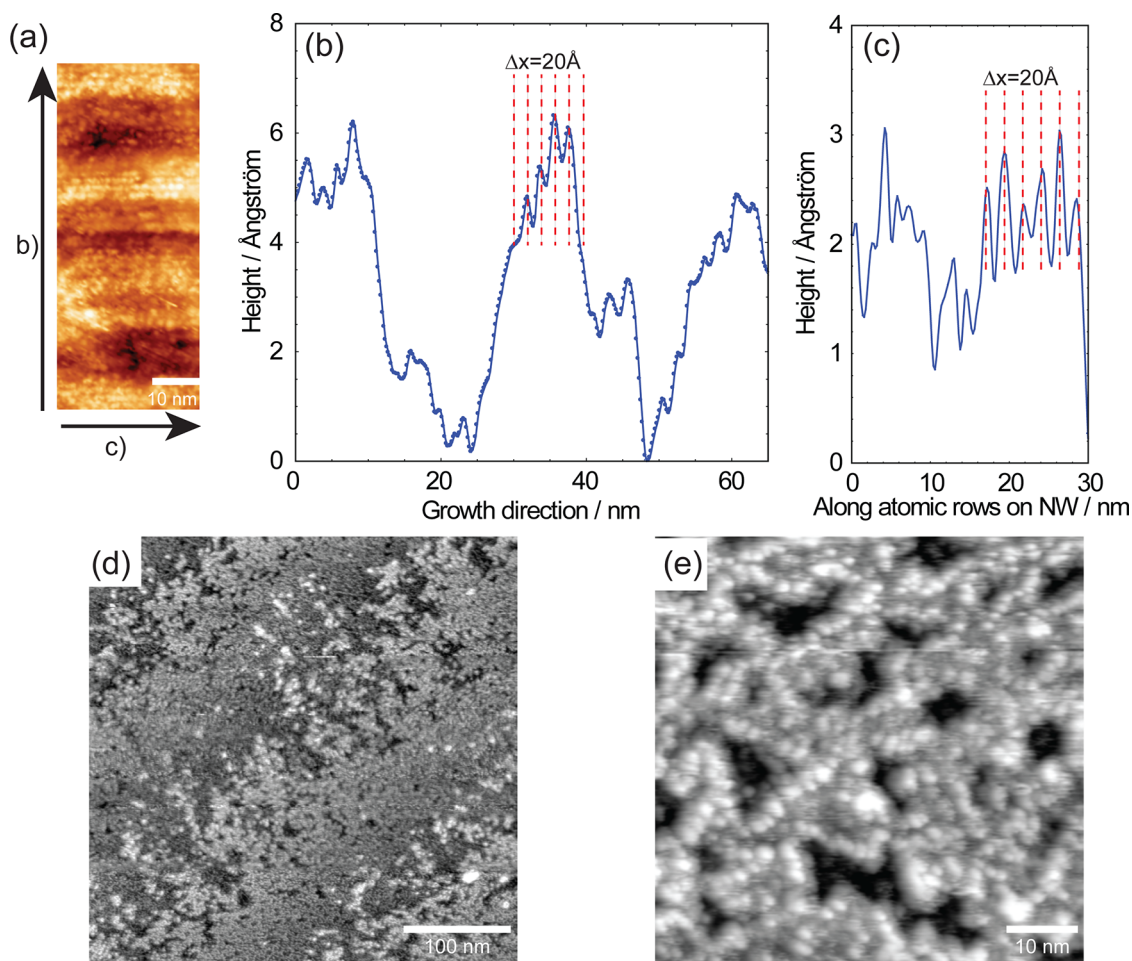
Figure 3. (a) STM image obtained at the n-part of an InP p-n junction NW depicting a disordered row structure, $U_{sample} = -3.0$ V. (b) Averaged height profile along the NW growth direction (the line marked b in panel a). (c) Height profile perpendicular to NW growth direction along a disordered row. (d,e) STM images obtained from atomic hydrogen-cleaned InP(111)B substrate, $U_{sample} = -3.0$ and -2.4 V for (d) and (e), respectively.

oxide clusters, or step edges on the NW. For comparing p- and n-type parts of the NWs, we obtained the spectra far away from the p-n interface in order to avoid the influence of the depletion region. At each position, 10−15 individual spectra were averaged. The STS results, depicting the local density of states (LDOS), from the cleaned InP(111)B, the n-type part, and the p-type part as well as from low-doped n-type (Sn) NWs ($n = 5 \times 10^{15}$ cm^{-3}) are shown in Figure 4. The valence and conduction band edges were determined by applying a linear extrapolation at the onset of the differential conductivity as was done previously by Feenstra and co-workers.[37] For the InP(111)B, we found a band gap of 1.40 eV and that the Fermi level was placed 0.65 eV from the valence band edge. The size of the band gap is consistent with the bulk value of 1.35 eV[38] at room temperature. The origin of the close to midgap Fermi level is considered likely to be due to Fermi level pinning induced by this surface being polar and reconstructed. Close to the conduction band onset, a region with nonzero conductivity can be seen which we propose is due to defect-induced acceptor states in the band gap.

For the n-type part, we observed a band gap of 1.53 eV and a Fermi level position at 0.3 eV below the conduction band edge (CB). The observed band gap was slightly larger than what would be expected for Wz InP, where the band gap at room temperature should be 1.43 eV.[38,39] STS measurements on unpinned semiconductor surfaces typically result in an enlarged band gap due to the effect of tip-induced band bending.[40,41] In order to quantitatively explain the observed deviation of the band gap, we simulated the effects of tip-induced band bending using the method of Feenstra et al.[42] Using reasonable model assumptions,[43] tip-induced band bending would result in an even slightly larger value for the band gap than 1.53 eV. Therefore, the measured band gap can be explained by a combination of tip-induced band bending and the presence of a small amount of surface states.

The Fermi level position at 0.3 eV below CB is, in a flat band situation, an indicator of a bulk charge carrier concentration of 1.5×10^{15} cm^{-3}, orders of magnitude lower than what was estimated from gate-dependent measurements (5×10^{18} cm^{-3}). This discrepancy in the
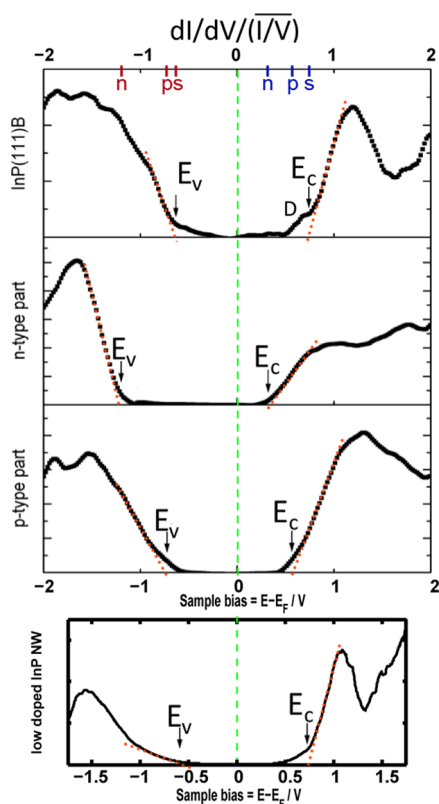
Figure 4. (dI/dV) / (I/V) spectra depicting the local density of states, obtained at the cleaned InP(111)B, n-type part of the pn-NW, p-type part of the pn-NW, and from low-doped n-type InP NW used as reference. The valence and conduction band edges were determined from linear extrapolations, indicated by the dotted orange lines, and are marked by E_v and E_c, respectively. The Fermi level can be found at 0 V sample bias (dashed green line). D marks defect-induced acceptor states. The markers in the top depict the placement of E_v and E_c for the n-part (n), p-part (p), and substrate (s).

position of the Fermi level with respect to the CB cannot be explained by tip-induced band bending as no reasonable parameters in the simulation change this value appreciably. The Fermi level could be pinned in position by, for example, steps which are unavoidable on NWs due to their hexagonal shape. We therefore repeated the experiment on low-doped n-type (Sn) NWs with a diameter of 80 nm which showed the same crystal structure. They showed similar band gap values as the n-type parts in the pn-NWs, but with the exception that the Fermi level was placed closer to the middle of the band gap (0.50 eV below CB) as would be expected for InP with lower donor concentration. From the measured band gap and position of the CB onset, we can conclude (1) that the n-type part of the clean surface is not completely Fermi level pinned but (2) that we are also not in a complete flat band situation as would be the case for ordinary clean Zb InP(110) surfaces. The observed partial pinning can well be explained by surface states induced by a reconstruction of the clean surface as indicated by the STM images presented above.
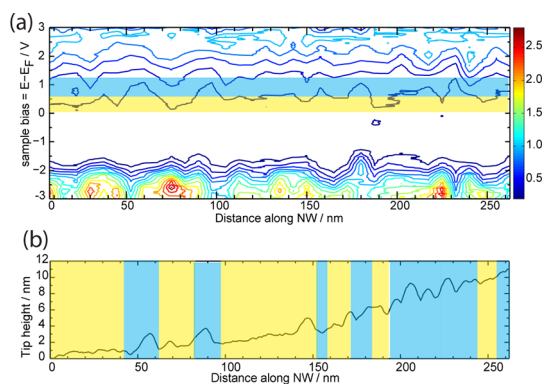

Figure 5. Axial evolution of the STS in the n-type part of the pn-NW along 250 nm. (a) STS data presented as a contour plot. Each column depicts tunneling spectra similar to those presented in Figure 4, where the increase in (dI/dV) / (I/V) amplitude is shown by the contours, with countour lines every 0.2 au. Each column is averaged over 10–15 spectra obtained with 7 nm distance along the pn-NW. The energy range slightly below and above the CB edge is colored yellow and blue, respectively. (b) Height profile along the NW obtained by STM. Positions at the NW where a significant density of states slightly below the CB edge (yellow range in panel a) is observed are also yellow colored in (b), while positions showing the lowest states slightly above the CB edge (blue in panel a) are blue colored in (b). A correlation to the surface roughness can be seen.

For the p-type part, a band gap of 1.32 eV was found and a Fermi level position at 0.76 eV from the valence band edge (VB). While the 1.32 eV band gap fits rather well with the band gap of Zb InP at room temperature, we note that taking tip-induced band bending into account this value is too low. This indicates that the surface band structure is indeed strongly influenced by surface states, presumably even more than the flat InP(111)B surface which shows a slightly larger band gap. Thus, it is no surprise that the midgap Fermi level observed is much different to the close to VB position that would be expected for a p-type material. The observed position of the Fermi level is completely dominated by surface states pinning the Fermi level. Thus we conclude that even the clean Zb part of the NW is strongly pinned at the surface, even more than the flat InP(111)B surface. This is not unexpected since the twinned Zb morphology in NWs is terminated by {111}A- and {111}B-type facets which are polar and thus expected to undergo reconstructions.[44] Finally, we note that our previous measurements on InAs indicated a metallic surface which we attributed to step- and defect-induced surface states.[17] On InP, we clearly have semiconducting behavior on the surface, but it appears that surface states inherent to the reconstruction still pin the Fermi level.

In order to spatially map out the electronic variations within a single NW, we performed STS at several positions in the n-type part of the pn-NW; see Figure 5. STS represents the only possibility to obtain the surface electronic structure across the NW with nanometer resolution. Each column depicts tunneling spectra similar

to those presented in Figure 4, where the increase in amplitude, equivalent to the LDOS, is shown by the contours. Each column is averaged over 10—15 spectra obtained at the same axial position along the NW. While the VB appears rather homogeneous, there is a variation along the NW for the lowest values near the CB edge which are consistent with additional defect-induced acceptor states. From the homogeneous VB, a specific influence of these defect states near the CB edge on the position of the Fermi level can be excluded. Surprisingly, the areas with less states below the CB edge are correlated with areas having a rougher morphology on a few nanometer scale. We note that there is also some correlation between the areas with more row ordering on the n-type structure and these roughly 20 nm wide hills. Thus these additional states could be attributed to atomic scale disorder on the surface of the NW.

In order to study long-range surface features of the pn-NWs, we used secondary electron (SE) X-ray photoelectron emission microscopy (XPEEM), as seen in Figure 6. SE XPEEM has been shown to be sensitive to dopant-induced contrast[45] and typically has a sampling depth of 5—10 nm and is therefore complementary to electron holography, for example, which is more bulk sensitive.[46,47] In this case, the observed SE contrast showed the n-type part as the brighter segment (Figure 6b). No qualitative changes in contrast were observed upon cleaning in atomic hydrogen or by changing the kinetic energy of the photoelectrons (Figure 6c). Even more complex structures in the form of double p-n junction NWs with a stacking of npnp were also grown and analyzed (Figure 6c—e). Note that these NWs were significantly longer than the single pn-NWs. The SE intensity from the n- and p-type parts of the npnp-NWs showed the same behavior as before with the n-type parts brightest. The dopant-induced contrast was once again unaffected by the deoxidation procedure. In addition, we observed in the SE measurements that the segment length was non-uniform, giving valuable feedback on the axial growth rate along the NW and the ability to grow longer superstructures of alternating p and n segments.

The low SE emission from p-type segments is opposite to what has been reported, both for bulk Si[48] and for n-type InP NWs.[45] In general, p-type areas have been observed as bright and gradually becoming darker as the p-doping decreases and darken further as the doping is set more and more n-type. In our measurements, it is apparent that the p-type part has a significantly lower SE yield and shows a shift of the SE spectrum toward higher kinetic energies by 60 meV (Figure 6f). We explain the low SE yield from the p-part by considering the effect of the highly abundant Zn atoms at the surface, which was obtained above. For highly Zn-doped InP, it is reported that the Zn atoms form Zn_3P_2 precipitates[49] or small Zn oxide/hydroxide inclusions. As Zn_3P_2 is unstable and oxidizes in contact
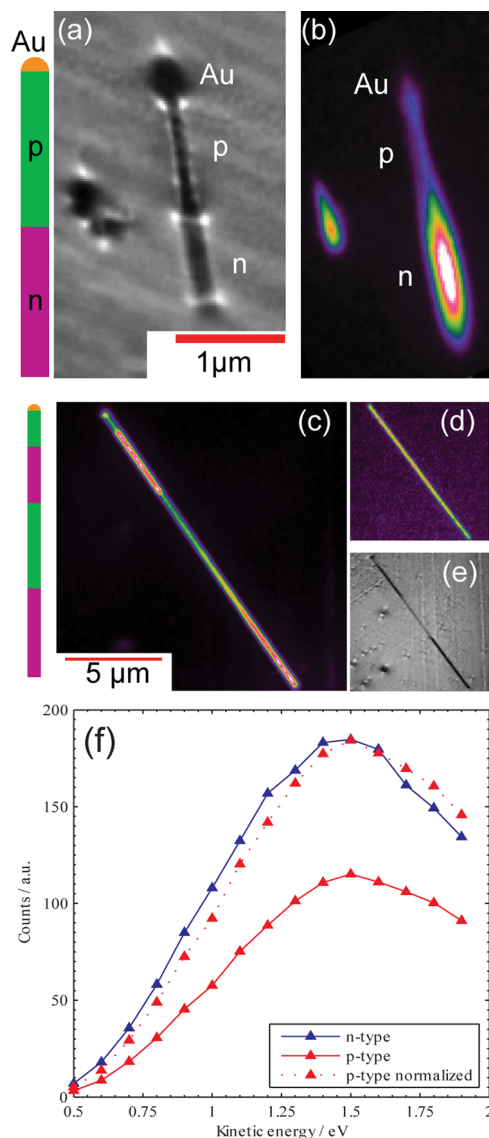

Figure 6. XPEEM imaging of InP pn- and pnpn-junction NWs cleaned in atomic hydrogen. (a) Mirror electron mode image showing a p-n junction NW. The Au particle can be found at the top followed by the p- and n-type segments (electron kinetic energy = 0.76 eV). (b) Secondary electron (SE) image of the same NW as in (a) with the different segments clearly visible ($h\nu$ = 100 eV, electron kinetic energy = 1.30 eV). (c) SE image of an pnpn-NW covered with native oxide; note the Au particle in the top left corner ($h\nu$ = 70 eV, electron kinetic energy = 0.28 eV). SE images of the NWs after cleaning look similar. (d) XPEEM image recorded using In4d photoelectrons ($h\nu$ = 70 eV, kinetic energy = 47.6 eV). (e) Mirror mode image of the NW after cleaning (kinetic energy = 0.13 eV). (f) Intensity of the n- (blue) and p-part (red) of the pn-NW as SEs with different kinetic energy are tuned in. The color code in (b,c) denotes the SE intensity with the n-type parts as the brightest.

with air,[50] the Zn precipitates are presumably mainly Zn oxides (which should be stable also under hydrogen cleaning at 400 °C). Such types of precipitates give rise to additional inelastic scattering hindering the SE emission and lowering the SE yield.

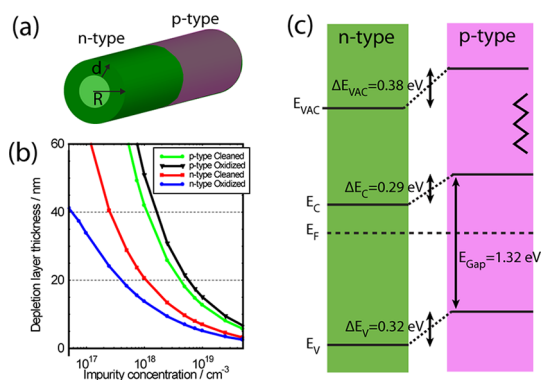To explain the shift of the SE peak, we follow the reasoning by Takeuchi et al., who studied SE emission

Figure 7. Using our multiple method approach, we arrive at a complete description of the InP p-n junction surface. (a) Schematic depiction of a pn-NW with radius R and depletion layer thickness d at the surface. (b) Obtained surface band bending for n-type and p-type NWs with/without oxide as a function of impurity concentration. For the p-type NWs, the depletion layer is thicker than the radius of the NW. (c) Surface band diagram of a p-n junction NW as derived from the combined STS and XPEEM data.

from metal crystals and found that the photoemission spectrum has a sharp onset at a minimum kinetic energy E_{k0} given by[51]

$$E_{k0} = \phi - eV_b - \phi_a$$

where ϕ is the work function of the sample, e is the elemental charge, V_b is the potential difference between the sample and the analyzer, and ϕ_a is the work function of the detector. For a semiconductor, the SEs are emitted from the densely occupied valence band rather than from the Fermi level and E_{k0} will thus be measured in relation to the valence band edge instead of the work function of the sample. In Figure 6f, we measured the shift in E_{k0} between the n- and p-type part to be 60 meV as measured between the parallel parts of the SE onset. The shift corresponds to (since V_b and ϕ_a are constant) the difference in ionization potential. With this information, we complete our knowledge of the surface band structure which is summarized in Figure 7c. We note that there is a difference in the electron affinity (conduction band edge to vacuum), where the p-part has a 90 meV larger electron affinity than the n-part, which we attribute to the difference in crystal structure. Differences in electron affinity are important since they will determine the possibilities of making Ohmic metal contacts to the semiconductor (in conjunction with the metal work function).

As we observe that the surfaces on both parts of the pn-NWs are (to some extent) Fermi level pinned, we can estimate a surface depletion layer thickness, d, close to the surface (or interface to the oxide) where significant band bending into the semiconductor occurs. We adopt the same method as in ref 4 and estimate d for a given doping concentration n and a surface Fermi level pinning potential ϕ_0, which is the difference between the Fermi level position in the bulk and at the surface. Assuming a cylindrical NW with

radius R, as sketched in Figure 7a, it is possible to estimate a minimum d by further assuming that $d \ll R$. The depletion layer width is given by[4]

$$\frac{4\pi\varepsilon_0\varepsilon\phi_0}{2\pi n} = \left(1 - \frac{d}{3R}\right)d^2$$

where ε_0 is the permittivity of vacuum and ε is the dielectric constant of the semiconductor (12.6 for InP). Using the knowledge we have on the oxidized and cleaned surfaces from XPS and STS, we can now estimate a minimum depletion layer thickness for different p- and n-doping levels with the result shown in Figure 7b. First it can be observed that for standard NWs with radii from 20 to 40 nm p-doping needs to be higher than 5×10^{18} cm^{-3} to achieve a situation where the surface pinning is not affecting the whole NW in a very significant fashion. As the oxide shell is n-type, even very low n-doping will result in a NW with n character; however, this can, on the other hand, limit how low n-doping can be achieved. Under the assumption that the p-type NWs have a bulk charge carrier concentration below 5×10^{17} cm^{-3}, we find that the surface Fermi level pinning potentials, with respect to VB, of 0.68 eV (cleaned NWs) and 1.10 eV (oxidized NWs) correspond to depletion layer widths larger than the NW radius R. These results show that a significant portion of the p-type NWs, especially when oxidized, will experience "n-type" behavior due to surface band bending extending into the NWs. However, since the pn-NWs show diode behavior,[29] a larger than expected amount of dopants must be present in the p-type part to screen the surface Fermi level pinning and give p-type characteristics. Indeed, the previously estimated low p-type carrier concentration for these NWs could be explained by the surface Fermi level pinning.

CONCLUSIONS

We have used a combination of XPS, XPEEM, LEEM, STM, and STS to gain a detailed, spatially resolved understanding of surface composition, band position changes, and morphology of InP NWs. Native oxide removal by atomic hydrogen was carefully monitored using XPS, and it was found that the oxides pin the surface Fermi level highly n-type, while other adsorbates have little effect. SE XPEEM imaging was used to observe doped segments in designed NWs with complex doping profiles. We measured the vacuum ionization differences between p- and n-type segments. Thus the complete band picture including the vacuum levels could be mapped out as shown in Figure 7c. Direct evidence of surface-related Zn at 0.2 monolayer coverage was found in XPS and XPEEM with indications that it was precipitated as oxidized Zn. Extensive STM investigations revealed surfaces with only local ordering, both for n-type NWs and for InP(111)B. A twinned Zb morphology could be related to p-type NWs. We can finally conclude that cleaning the surface from

native oxides formed during exposure to ambient air leads to a partial unpinning of the surface, making it easier to control the surface using dopant incorporation during synthesis. However it is important, for continued miniaturization, to control the extent of the surface band bending even better and make sure that one Fermi level pinning is not just replaced by another one upon removal of the oxide. Thus chemical tailoring of NW surfaces in combination with careful monitoring of the effect will be needed.

EXPERIMENTAL METHODS

Au-catalyzed homogenously doped InP NWs (80 nm thick) were grown in a metal organic chemical vapor deposition (MOCVD) reactor using dimethylzinc (DMZn) as p-type precursor and tetraethyltin (TESn) or hydrogen sulfide (H_2S) as n-type precursor. NW tapering was controlled by in situ etching using HCl.[52] Homogenously doped n-type (Sn) NWs showed charge carrier concentrations ranging from $n = 5 \times 10^{15}$ to $n = 5 \times 10^{18}$ cm^{-3}, whereas the p-type NWs showed clear p-type behavior, but the charge carrier concentrations were too low to be determined using gate-dependent measurements (devices normally off). NWs with axial stacking of n-p and n-p-n-p segments were grown using DMZn and TESn flows matching the highest obtained carrier concentrations. More details on growth can be found in ref.[29] DMZn induced a periodically twinned zinc blende (Zb) crystal structure as previously reported.[32] The TESn, on the other hand, was not seen to affect the crystal structure and the NWs showed predominantly wurtzite (Wz) structure with plenty of stacking faults. Sulfur was seen to induce a pure Wz stacking. The NWs were grown free-standing on epi-ready InP(111)B wafers and were broken off to investigate the side facets. NWs for XPEEM were deposited on HF-etched Si using a clean room paper to transfer the NWs from the growth substrate resulting in a sparse coverage of NWs. For XPS, a high density of NWs was required in order to obtain a high signal-to-noise ratio. For this purpose, dense assemblies of uniformly doped NWs were deposited on HF-etched Si using a dry deposition method as described elsewhere.[5] For the STM studies, the NWs were transferred to a sulfur-doped, $n = 3 \times 10^{18}$ cm^{-3} epi-ready InP(111)B substrate.

X-ray photoelectron emission microscopy/spectroscopy (XPEEM/XPS) was performed at the soft X-ray beamline I311 at the MAX IV laboratory in Lund, Sweden, using an Elmitec SPELEEM III and a Scienta SES200 analyzer for XPEEM and XPS, respectively, operating at a pressure $p < 10^{-10}$ mbar in room temperature. The energy of the X-rays was in between 70 and 1330 eV. In XPEEM, it has been shown that improved reliability in the experimental data can be obtained if the SEs are analyzed with respect to kinetic energy instead of the total yield.[53] All experiments presented within this paper were therefore performed using an electron energy analyzer measuring the number of photoelectrons as a function of kinetic energy. An ultrahigh vacuum (UHV) Omicron XA VT STM operated at a pressure $p < 10^{-10}$ mbar in room temperature was used for the STM studies. STS was used to probe the surface electronic structure of the cleaned InP NWs and the InP(111)B substrate. During acquisition, the tip was moved closer to the surface with 2 Å/|V| in order to increase the sensitivity at low sample bias, according to the so-called Feenstra mode.[37] In the graphs, the numerically differentiated conductance has been normalized to the total conductance broadened by an exponential function which has been shown to be a suitable way to give a representation of the local density of states (LDOS) and removing height correlated differences introduced by the Feenstra mode.[54] For the STS data presented in Figure 5, we used a lock-in technique to directly obtain the differentiated conductance.

The NWs were analyzed both covered with native oxide from exposure to ambient air and after oxide removal in vacuum. In the deoxidation procedure, the NWs were heated to 400 °C and exposed to a beam of atomic hydrogen. Different cleaning times varying between 2 and 40 min were compared, typically in steps of 8 min. For more information about deoxidation of III–V NWs, see ref 17. Spatially resolved XPS (μXPS), obtained within the XPEEM system, of the cleaned NWs were compared to spectra obtained for homogenously doped NWs using the high-resolution XPS setup at beamline I311 at the MAX IV laboratory, Lund, to ensure similar surface conditions.

REFERENCES AND NOTES

1. Wallentin, J.; Borgström, M. T. Doping of Semiconductor Nanowires. *J. Mater. Res.* **2011**, *26*, 2142–2156.
2. van Weert, M. H. M.; Helman, A.; van den Einden, W.; Algra, R. E.; Verheijen, M. A.; Borgström, M. T.; Immink, G.; Kelly, J. J.; Kouwenhoven, L. P.; Bakkers, E. P. A. M. Zinc Incorporation via the Vapor−Liquid−Solid Mechanism into InP Nanowires. *J. Am. Chem. Soc.* **2009**, *131*, 4578–4579.
3. Perea, D. E.; Hemesath, E. R.; Schwalbach, E. J.; Lensch-Falk, J. L.; Voorhees, P. W.; Lauhon, L. J. Direct Measurement of Dopant Distribution in an Individual Vapour−Liquid−Solid Nanowire. *Nat. Nanotechnol.* **2009**, *4*, 315–319.
4. Wang, D.; Chang, Y.-L.; Wang, Q.; Cao, J.; Farmer, D. B.; Gordon, R. G.; Dai, H. Surface Chemistry and Electrical Properties of Germanium Nanowires. *J. Am. Chem. Soc.* **2004**, *126*, 11602–11611.
5. Timm, R.; Hjort, M.; Fian, A.; Borg, B. M.; Thelander, C.; Andersen, J. N.; Wernersson, L. E.; Mikkelsen, A. Interface Composition of InAs Nanowires with Al_2O_3 and HfO_2 Thin Films. *Appl. Phys. Lett.* **2011**, *99*, 222907.
6. Cui, Y.; Lieber, C. M. Functional Nanoscale Electronic Devices Assembled Using Silicon Nanowire Building Blocks. *Science* **2001**, *291*, 851–853.
7. Law, M.; Goldberger, J.; Yang, P. D. Semiconductor Nanowires and Nanotubes. *Annu. Rev. Mater. Res.* **2004**, *34*, 83–122.
8. Borgström, M. T.; Wallentin, J.; Heurlin, M.; Fält, S.; Wickert, P.; Leene, J.; Magnusson, M. H.; Deppert, K.; Samuelson, L. Nanowires With Promise for Photovoltaics. *IEEE J. Sel. Top. Quantum Electron.* **2011**, *17*, 1050–1061.
9. Svensson, C. P. T.; Mårtensson, T.; Trägårdh, J.; Larsson, C.; Rask, M.; Hessman, D.; Samuelson, L.; Olsson, J. Monolithic GaAs/InGaP Nanowire Light Emitting Diodes on Silicon. *Nanotechnology* **2008**, *19*, 305201.
10. Duan, X. F.; Huang, Y.; Cui, Y.; Wang, J. F.; Lieber, C. M. Indium Phosphide Nanowires as Building Blocks for Nanoscale Electronic and Optoelectronic Devices. *Nature* **2001**, *409*, 66–69.
11. Garnett, E. C.; Tseng, Y.-C.; Khanal, D. R.; Wu, J.; Bokor, J.; Yang, P. Dopant Profiling and Surface Analysis of Silicon Nanowires Using Capacitance-Voltage Measurements. *Nat. Nanotechnol.* **2009**, *4*, 311–314.

12. Zhang, S.; Hemesath, E. R.; Perea, D. E.; Wijaya, E.; Lensch-Falk, J. L.; Lauhon, L. J. Relative Influence of Surface States and Bulk Impurities on the Electrical Properties of Ge Nanowires. *Nano Lett.* **2009**, *9*, 3268–3274.

13. Ouattara, L.; Mikkelsen, A.; Sköld, N.; Eriksson, J.; Knaapen, T.; Cavar, E.; Seifert, W.; Samuelson, L.; Lundgren, E. GaAs/AlGaAs Nanowire Heterostructures Studied by Scanning Tunneling Microscopy. *Nano Lett.* **2007**, *7*, 2859–2864.

14. Lüth, H. *Surfaces and Interfaces of Solids*; Springer-Verlag: Berlin, 1993.

15. Soci, C.; Zhang, A.; Xiang, B.; Dayeh, S. A.; Aplin, D. P. R.; Park, J.; Bao, X. Y.; Lo, Y. H.; Wang, D. ZnO Nanowire UV Photodetectors with High Internal Gain. *Nano Lett.* **2007**, *7*, 1003–1009.

16. Xu, T.; Dick, K. A.; Plissard, S.; Nguyen, T. H.; Makoudi, Y.; Berthe, M.; Nys, J. P.; Wallart, X.; Grandidier, B.; Caroff, P. Faceting, Composition and Crystal Phase Evolution in III–V Antimonide Nanowire Heterostructures Revealed by Combining Microscopy Techniques. *Nanotechnology* **2012**, DOI: 10.1088/0957-4484/23/9/095702.

17. Hilner, E.; Håkanson, U.; Fröberg, L. E.; Karlsson, M.; Kratzer, P.; Lundgren, E.; Samuelson, L.; Mikkelsen, A. Direct Atomic Scale Imaging of III–V Nanowire Surfaces. *Nano Lett.* **2008**, *8*, 3978–3982.

18. Allen, J. E.; Perea, D. E.; Hemesath, E. R.; Lauhon, L. J. Nonuniform Nanowire Doping Profiles Revealed by Quantitative Scanning Photocurrent Microscopy. *Adv. Mater.* **2009**, *21*, 3067.

19. Leonard, F.; Talin, A. A. Electrical Contacts to One- and Two-Dimensional Nanomaterials. *Nat. Nanotechnol.* **2011**, *6*, 773–783.

20. den Hertog, M. I.; Schmid, H.; Cooper, D.; Rouviere, J.-L.; Björk, M. T.; Riel, H.; Rivallin, P.; Karg, S.; Riess, W. Mapping Active Dopants in Single Silicon Nanowires Using Off-Axis Electron Holography. *Nano Lett.* **2009**, *9*, 3837–3843.

21. Oigawa, H.; Fan, J. F.; Nannichi, Y.; Sugahara, H.; Oshima, M. Universal Passivation Effect of $(NH_4)_2S_x$ Treatment on the Surface of III–V Compound Semiconductors. *Jpn. J. Appl. Phys., Part 2* **1991**, *30*, L322–L325.

22. Eymery, J.; Favre-Nicolin, V.; Fröberg, L.; Samuelson, L. X-ray Measurements of the Strain and Shape of Dielectric/Metallic Wrap-Gated InAs Nanowires. *Appl. Phys. Lett.* **2009**, *94*, 131911.

23. Wallentin, J.; Persson, J. M.; Wagner, J. B.; Samuelson, L.; Deppert, K.; Borgström, M. T. High-Performance Single Nanowire Tunnel Diodes. *Nano Lett.* **2010**, *10*, 974–979.

24. Losurdo, M.; Capezzuto, P.; Bruno, G. Study of the H2 Remote Plasma Cleaning of InP Substrate for Epitaxial Growth. *J. Vac. Sci. Technol., B* **1996**, *14*, 691–697.

25. Gallet, D.; Hollinger, G.; Santinelli, C.; Goldstein, L. *In Situ* Characterization of InP Surfaces after Low-Energy Hydrogen Ion Cleaning. *J. Vac. Sci. Technol., B* **1992**, *10*, 1267–1272.

26. Bertness, K. A.; Kendelewicz, T.; List, R. S.; Williams, M. D.; Lindau, I.; Spicer, W. E. Fermi Level Pinning During Oxidation of Atomically Clean n-InP(110). *J. Vac. Sci. Technol., A* **1986**, *4*, 1424–1426.

27. Hollinger, G.; Bergignat, E.; Joseph, J.; Robach, Y. On the Nature of Oxides on InP Surfaces. *J. Vac. Sci. Technol., A* **1985**, *3*, 2082–2088.

28. Ho, C. P.; Plummer, J. D. Si/SiO₂ Interface Oxidation Kinetics: A Physical Model for the Influence of High Substrate Doping Levels. *J. Electrochem. Soc.* **1979**, *126*, 1516–1522.

29. Borgström, M. T.; Norberg, E.; Wickert, P.; Nilsson, H. A.; Trägårdh, J.; Dick, K. A.; Statkute, G.; Ramvall, P.; Deppert, K.; Samuelson, L. Precursor Evaluation for *In Situ* InP Nanowire Doping. *Nanotechnology* **2008**, *19*, 445602.

30. Yeh, J. J.; Lindau, I. Atomic Subshell Photoionization Cross Sections and Asymmetry Parameters: $1 \leq Z \leq 103$. *At. Data Nucl. Data Tables* **1985**, *32*, 1–155.

31. Kuphal, E. Preparation and Characterization of LPE InP. *J. Cryst. Growth* **1981**, *54*, 117–126.

32. Algra, R. E.; Verheijen, M. A.; Borgström, M. T.; Feiner, L. F.; Immink, G.; van Enckevort, W. J. P.; Vlieg, E.; Bakkers, E. P. A. M. Twinning Superlattices in Indium Phosphide Nanowires. *Nature* **2008**, *456*, 369–372.

33. Kamiya, I.; Aspnes, D. E.; Florez, L. T.; Harbison, J. P. Reflectance-Difference Spectroscopy of (001) GaAs Surfaces in Ultrahigh Vacuum. *Phys. Rev. B* **1992**, *46*, 15894–15904.

34. Schmidt, W. G. III–V Compound Semiconductor (001) Surfaces. *Appl. Phys. A: Mater. Sci. Process.* **2002**, *75*, 89.

35. Hilner, E.; Lundgren, E.; Mikkelsen, A. Surface Structure and Morphology of InAs(111)B with/without Gold Nanoparticles Annealed under Arsenic or Atomic Hydrogen Flux. *Surf. Sci.* **2010**, *604*, 354–360.

36. Hilner, E.; Mikkelsen, A.; Eriksson, J.; Andersen, J. N. Lundgren, E.; Zakharov, A.; Yi, H.; Kratzer, P. Au Wetting and Nanoparticle Stability on GaAs(111)B. *Appl. Phys. Lett.* **2006**, *89*, 251912.

37. Feenstra, R. M. Tunneling Spectroscopy of the (110)-Surface of Direct-Gap III–V Semiconductors. *Phys. Rev. B* **1994**, *50*, 4561–4570.

38. Pavesi, L.; Piazza, F.; Rudra, A.; Carlin, J. F.; Ilegems, M. Temperature Dependence of the InP Band Gap from a Photoluminescence Study. *Phys. Rev. B* **1991**, *44*, 9052–9055.

39. Tuin, G.; Borgström, M.; Trägårdh, J.; Ek, M.; Wallenberg, L.; Samuelson, L.; Pistol, M.-E. Valence Band Splitting in Wurtzite InP Nanowires Observed by Photoluminescence and Photoluminescence Excitation Spectroscopy. *Nano Res.* **2011**, *4*, 159–163.

40. Feenstra, R. M.; Lee, J. Y.; Kang, M. H.; Meyer, G.; Rieder, K. H. Band Gap of the Ge(111)c(2 × 8) Surface by Scanning Tunneling Spectroscopy. *Phys. Rev. B* **2006**, *73*, 035310.

41. Timm, R.; Feenstra, R. M.; Eisele, H.; Lenz, A.; Ivanova, L.; Lenz, E.; Dahne, M. Contrast Mechanisms in Cross-Sectional Scanning Tunneling Microscopy of GaSb/GaAs Type-II Nanostructures. *J. Appl. Phys.* **2009**, *105*, 093718.

42. Feenstra, R. M.; Gaan, S.; Meyer, G.; Rieder, K. H. Low-Temperature Tunneling Spectroscopy of Ge(111)c(2 × 8) Surfaces. *Phys. Rev. B* **2005**, *71*, 125316.

43. In the calculations, a tip radius of 10 nm and tip–sample distance of 1.0 nm were used. No contact potential between tip and sample was applied. For doping levels and dielectric constants, nominal values were used.

44. Hansson, G. V.; Uhrberg, R. I. G. Photoelectron Spectroscopy of Surface States on Semiconductor Surfaces. *Surf. Sci. Rep.* **1988**, *9*, 197–292.

45. Hjort, M.; Wallentin, J.; Timm, R.; Zakharov, A. A.; Andersen, J. N.; Samuelson, L.; Borgström, M. T.; Mikkelsen, A. Doping Profile of InP Nanowires Directly Imaged by Photoemission Electron Microscopy. *Appl. Phys. Lett.* **2011**, *99*, 233113.

46. Chung, S.; Johnson, S. R.; Zhang, Y.-H.; Smith, D. J.; McCartney, M. R. Off-Axis Electron Holographic Potential Mapping Across AlGaAs/AlAs/GaAs Heterostructures. *J. Appl. Phys.* **2009**, *105*, 014910.

47. Cooper, D.; Truche, R.; Twitchett-Harrison, A. C.; Dunin-Borkowski, R. E.; Midgley, P. A. Quantitative Off-Axis Electron Holography of GaAs p-n Junctions Prepared by Focused Ion Beam Milling. *J. Microsc.* **2009**, *233*, 102–113.

48. Sealy, C. P.; Castell, M. R.; Wilshaw, P. R. Mechanism for Secondary Electron Dopant Contrast in the SEM. *J. Electron Microsc.* **2000**, *49*, 311–321.

49. Frigeri, C.; Ferrari, C.; Fornari, R.; Weyher, J. L.; Longo, F.; Guadalupi, G. M. Structural Characterization of Heavily Zn-Doped Liquid Encapsulated Czochralski InP. *Mater. Sci. Eng., B* **1994**, *28*, 120–125.

50. Elrod, U.; Luxsteiner, M. C.; Obergfell, M.; Bucher, E.; Schlapbach, L. Surface-Chemistry of Zn3P3 Single-Crystals Studied by XPS. *Appl. Phys. B* **1987**, *43*, 197–201.

51. Takeuchi, K.; Suda, A.; Ushioda, S. Local Variation of the Work Function of Cu(1;1;1) Surface Deduced from the Low Energy Photoemission Spectra. *Surf. Sci.* **2001**, *489*, 100–106.

52. Borgström, M. T.; Wallentin, J.; Trägårdh, J.; Ramvall, P.; Ek, M.; Wallenberg, L. R.; Samuelson, L.; Deppert, K. *In Situ* Etching for Total Control over Axial and Radial Nanowire Growth. *Nano Res.* **2010**, *3*, 264–270.

53. Kazemian, P.; Mentink, S. A. M.; Rodenburg, C.; Humphreys, C. J. High Resolution Quantitative Two-Dimensional Dopant Mapping Using Energy-Filtered Secondary Electron Imaging. *J. Appl. Phys.* **2006**, *100*, 054901.

54. Mårtensson, P.; Feenstra, R. M. Geometric and Electronic-Structure of Antimony on the GaAs(110) Surface Studied by Scanning Tunneling Microscopy. *Phys. Rev. B* **1989**, *39*, 7744–7753.